Fundamentals of Electron Beam Exposure and Development

2

Mohammad Ali Mohammad, Mustafa Muhammad, Steven K. Dew, and Maria Stepanova

Abstract

Electron Beam Lithography (EBL) is a fundamental technique of nanofabrication, allowing not only the direct writing of structures down to sub-10 nm dimensions, but also enabling high volume nanoscale patterning technologies such as (DUV and EUV) optical lithography and nanoimprint lithography through the formation of masks and templates. This chapter summarizes the key principles of EBL and explores some of the complex interactions between relevant parameters and their effects on the quality of the resulting lithographic structures. The use of low energy exposure and cold development is discussed, along with their impacts on processing windows. Applications of EBL are explored for the fabrication of very small isolated bridge structures and for high density master masks for nanoimprint lithography. Strategies for using both positive and negative tone resists are explored.

2.1 Introduction

With its ability to form arbitrary two-dimensional patterns down to the nanometer scale, electron beam lithography (EBL) is one of the most important techniques in nanofabrication. In short, it involves the exposure by a highly focused electron

M.A. Mohammad (✉) • M. Muhammad • S.K. Dew
Department of Electrical and Computer Engineering, University of Alberta, Edmonton, AB, Canada
e-mail: M.A.Mohammad@ualberta.net

M. Stepanova
National Institute for Nanotechnology, National Research Council, and Department of Electrical and Computer Engineering, University of Alberta, Edmonton, AB, Canada

M. Stepanova and S. Dew (eds.), *Nanofabrication*,
DOI 10.1007/978-3-7091-0424-8_2, © Springer-Verlag/Wien 2012

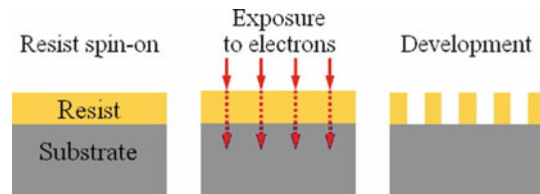

Fig. 2.1 Outline of EBL process steps to form a nanoscale pattern in a positive-tone resist layer

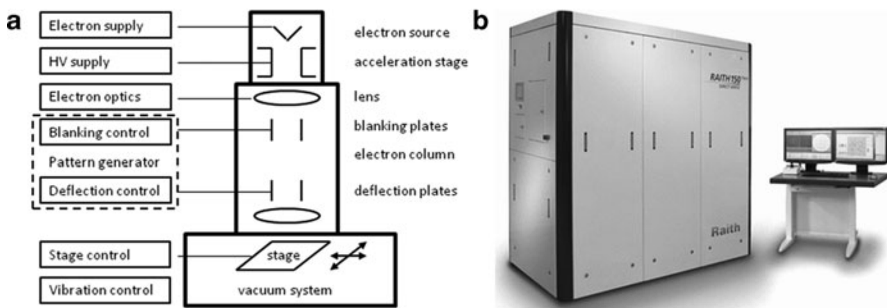

Fig. 2.2 Electron beam exposures systems: (**a**) schematic diagram, (**b**) Raith 150^{TWO} commercial EBL system (used with permission [7])

beam to dramatically modify the solubility of a resist material during a subsequent development step, see Fig. 2.1.

EBL was originally developed using scanning electron microscopes to which a pattern generator and beam blanker was added to control which areas of the viewing field are exposed [1–3] (see Fig. 2.2a for a schematic description of an EBL system). Modern EBL tools are fully dedicated patterning systems (Fig. 2.2b) that employ high brightness electron sources for faster throughput and high resolution mechanical stages to be able to expose step-by-step large substrates under the relatively narrow field of focus of the electron beam. These direct write systems have the advantage of extremely high resolution and the ability to create arbitrary patterns without a mask. Their disadvantage is the long times taken to write large, complex patterns. Efforts to overcome this challenge include projection EBL [4, 5] and the use of massively parallel beams [6]. Due to the developmental stage of these latter techniques, however, this chapter will focus on the single beam, direct write EBL technique.

The key objectives of EBL writing are to achieve arbitrary patterns in the resist with high resolution, high density, high sensitivity and high reliability. These characteristics are interrelated in a complex fashion. The key determinants will be the quality of the electron optics (e.g., the ability to create a finely focused spot), the choice of resist, substrate and developer, and the process conditions: electron beam energy and dose, and development time and temperature. Factors that complicate these objectives are delocalization of electrons due to forward and backscattering (proximity effects), collapse of the pattern due to swelling and capillarity forces, and fluctuations in the sizes of features (line edge roughness).

2.1.1 Electron Transport

The first requirement for a high quality beam is a stable, high brightness electron source, such as one employing thermal field emission. The quality of the spot is determined by the electron optics and degree of focus. It is necessary to have high positional accuracy with limited astigmatism and small spot size [8]. The electron column is under vacuum to reduce gas scattering of the beam, but divergence of the beam does result from mutual electrostatic repulsion by the electrons. This effect is more pronounced at higher currents and lower energies. Notwithstanding this, commercial EBL systems can usually deliver a spot size of just a few nanometers [7, 9, 10]. Unfortunately, other factors such as scattering will usually limit the final resist pattern to a larger size.

As the electrons enter the resist, they begin a series of low energy elastic collisions, each of which will deflect the electron slightly. This forward scattering broadens the beam by an amount that increases with thickness, and this effect is more pronounced at low incident energies [11, 12] (see also Fig. 2.3).

In addition to forward scattering, there is also backscattering to consider [13]. Typically, most of the electrons pass entirely through the resist and penetrate deeply into the substrate. Some fraction of those electrons will eventually undergo enough large angle collisions to re-emerge into the resist at some distance from the point at which they left it (see Fig. 2.4). At higher energies, these backscattered electrons may cause exposure microns away [14, 15] from where the beam entered. This leads to the so-called proximity effect [16–18] where electrons writing a feature at one location increase the exposure at a nearby feature, causing pattern distortion and overexposure. The density of features becomes an important factor in determining necessary exposure levels. Backscattering can be minimized by exposing on a thin membrane substrate.

Another electron transport consideration is secondary electrons [1]. These are low energy (a few to a few tens of eV) electrons produced by ionizations resulting from inelastic collisions by the primary incident electrons [19]. Because of their

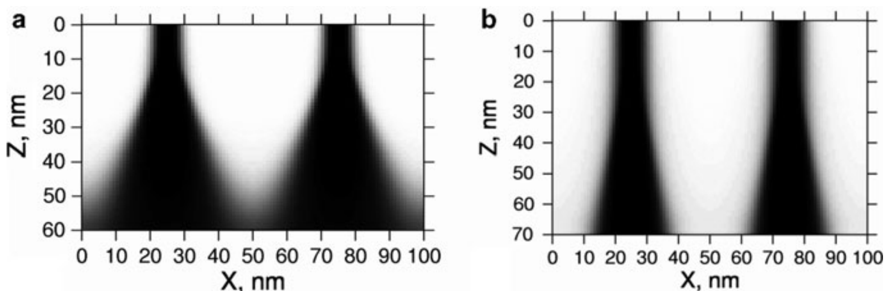

Fig. 2.3 Electron beam broadening due to forward scattering in the resist at (**a**) 3 keV and (**b**) 10 keV of incident energy. Shown is a predicted cross-section of resist exposure for two parallel lines

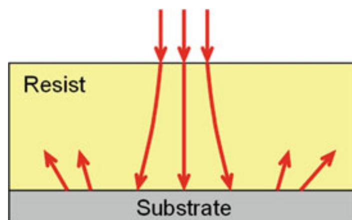

Fig. 2.4 Forward and backscattering of electrons in the resist and substrate leading to beam broadening and proximity effects

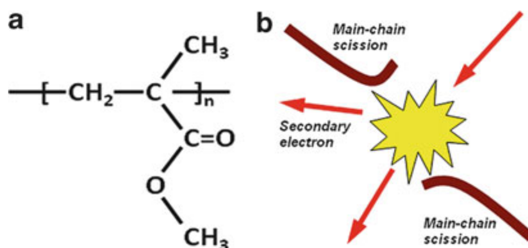

Fig. 2.5 (**a**) Polymer subunit of poly (methyl methacrylate), and (**b**) scission of the polymer chain during EBL exposure

energy, secondary electrons have short range (several nanometers) but may ultimately limit the resolution possible with EBL.

A final transport issue is electrostatic charging, particularly if writing onto an insulating substrate. If there exists no pathway for the absorbed electrons to dissipate, charge will build up and defocus the electron beam. In such cases, a thin metal [1] or conductive polymer [20] layer is required above or below the resist.

2.1.2 EBL Resists

Inelastic collisions of electrons with the resist result in ionization (secondary electron generation), which is accompanied by physico-chemical changes in the resist. Just as with optical lithography, EBL can employ two classes of resist. Positive tone resists undergo a conversion from low to high solubility upon exposure to electrons. The classic example is PMMA (poly-methyl methacrylate) which is a long chain polymer (Fig. 2.5a) that is broken into smaller, more soluble fragments by the electron beam (Fig. 2.5b) [21]. Another common positive resist is ZEP 520 which also consists of a long chain polymer [22, 23].

In a negative tone resist, the electrons convert the material to low solubility. The prime example here would be HSQ (hydrogen silsesquioxane) which undergoes a cross-linking reaction to combine smaller polymers into larger, less soluble ones [24]. Several other negative resists have been recently compared [25].

The most common positive resist, PMMA, consists of very long polymer chains with masses of 496 and 950 kDa being common. With such long chains, it takes many scission events before the resulting fragments become significantly soluble.

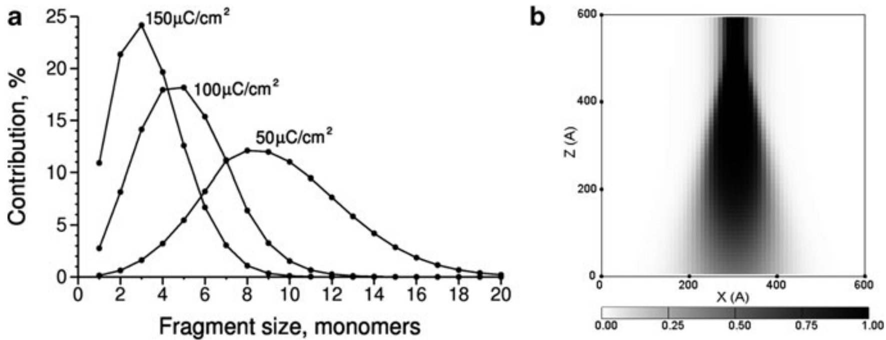

Fig. 2.6 (**a**) Calculated distribution of PMMA fragment sizes for various doses at 10 keV [26]. (**b**) Spatial distribution of the volume fraction of small (less than 10 monomers) fragments within the resist due to exposure at a single point

Hence, the distribution of fragment sizes becomes an important factor in understanding the relationship between exposure dose and development behavior. Figure 2.6a shows the distribution of PMMA fragment sizes and exposure dose [26]. As dose increases, the average fragment size decreases and solubility in the developer increases. Of course, dose varies spatially because of scattering, so the 3D distribution of scission events (Fig. 2.6b) becomes an important component to this total picture. Similar considerations also apply to other resists – positive or negative.

2.1.3 Resist Development

After exposure, the resist is typically immersed in a liquid developer to dissolve the fragments (positive tone) or non-crosslinked molecules (negative tone). Temperature and duration become important parameters here as the hotter/longer the development, the farther along the continuum of solubility the dissolution extends. For example, cold development of PMMA (discussed below) freezes out the development of all but the very smallest fragments, resulting in very high resolution as much of the scattered electrons cause insufficient exposure to reach this threshold.

During development, the solvent penetrates into the polymer matrix and starts to surround the fragments. As the molecules start to interact, a gel is formed (see Fig. 2.7). The thickness of the gel layer will depend on the amount of fragmentation and the strength of the solvent. Swelling of the polymer can also result. Once completely surrounded by solvent, the fragments detach from the matrix and diffuse into the solvent. Longer fragments are less mobile and more strongly bound to the matrix and take longer to dissolve [27–29]. More powerful solvents will remove longer fragments which is not always desirable if high resolution is required. Exposure and development are interrelated as short exposure with long or aggressive development can be equivalent to heavier exposure with short development.

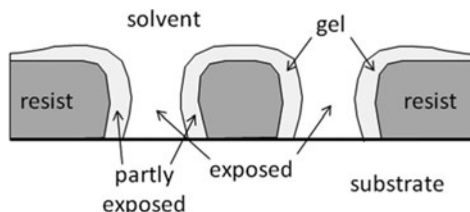

Fig. 2.7 Positive resist during development. Polymer-solvent interactions can result in gel formation and swelling

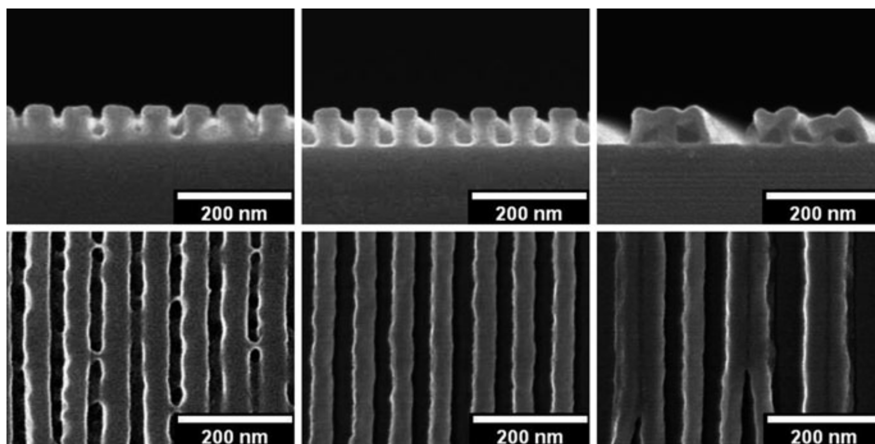

Fig. 2.8 PMMA grating structures in cross-section (*top*) and plan view (*bottom*). Shown are underexposed/underdeveloped (*left*), quality structures (*middle*) and collapsed patterns (*right*) [31]

This can lead to some ambiguity between the terms underdeveloped and underexposed or overdeveloped and overexposed. As will be discussed further below, the kinetics of the dissolution process becomes quite important to the optimization of EBL necessitating understanding of these factors at a detailed level. Often a mix of solvents (such as 1:3 methyl isobutyl ketone with isopropyl alcohol for PMMA) is used to tailor dissolution behavior.

An issue that arises if the resist is overdeveloped is the degradation of the resist-substrate bond and the capillarity forces that result as the solvent is removed. These lead to the mechanical failure of the resist structure resulting in pattern collapse [30]. Adjacent linear features are particularly vulnerable to this problem, especially for thick resists. Figure 2.8 shows examples of pattern collapse, along with underexposed/underdeveloped structures in PMMA.

2.1.4 Process Parameters

As has been implied above, there is a large number of parameters affecting the EBL process in a complex, interacting fashion. A partial list is given in Table 2.1. This

Table 2.1 Parameters affecting the EBL process

Parameter	Process impact
Exposure energy	Resolution, sensitivity, proximity
Exposure dose	Pattern quality
Pattern density	Proximity, pattern quality
Resist material	Sensitivity, resolution, contrast
Resist thickness	Sensitivity, resolution, pattern quality
Developer	Sensitivity, resolution, development window
Development temperature	Sensitivity, resolution, exposure window
Development time	Sensitivity, resolution, exposure window

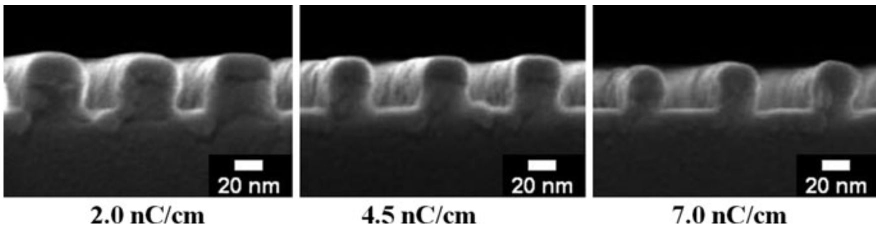

Fig. 2.9 Cross sectional profiles in 70 nm pitch PMMA gratings fabricated using 30 keV voltage and various line doses. The samples were developed at −15°C for 15 s, and the initial PMMA thickness was 55 nm [38]

excludes secondary factors such as resist polymer chain length which can impact sensitivity and contrast, or the use of techniques such as ultrasonic agitation [32–34] to reduce development times and improve clearance, or the use of critical point drying [35–37] to minimize pattern collapse. Of course, the objective of manipulating these parameters is to achieve a high resolution, high quality, high throughput result with large process windows to maximize yield and reproducibility.

An example of some of these process dependencies can be seen in Fig. 2.9 which shows the effect of dose on a single pixel line grating. While the structures are well-resolved at all three doses, the size of the final structures varies significantly. Similarly, Fig. 2.10 summarizes the aspect ratio (height:width) of the features resulting as a function of dose. The complexity of these interactions drives the need for better understanding and modelling techniques (see Chap. 3) for the optimization of EBL processes.

2.2 Process Windows with PMMA Resist

As requirements for lithography have progressed toward the sub-20 nm regime, major challenges have emerged for introducing controllable radiation-induced changes at molecular-size scales. Novel EBL processes that would extend capabilities of the technology significantly into the deep nanoscale regime entail

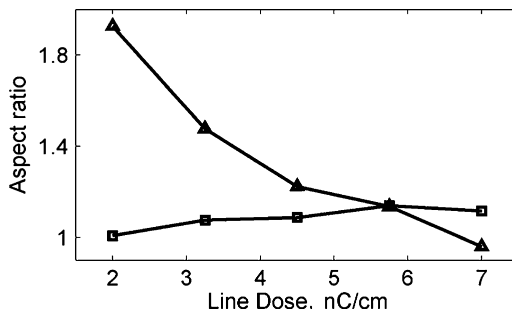

Fig. 2.10 Aspect ratios for the interline gaps (*triangles*) and PMMA lines (*squares*) as a function of the exposure dose, determined from cross-sectional SEM images for 70 nm pitch gratings fabricated using 30 keV electrons. Other process conditions were as in Fig. 2.9 [38]

new approaches to resist design, exposure strategies, and development techniques [31, 38–43]. To achieve this will require thorough, systematic understanding of the limiting factors [44] involved in both the electron-resist interaction and in the polymer dissolution (development), as well as the corresponding intricate interplay of the numerous process control parameters including the accelerating voltage, exposure dose, and development conditions.

Due to the proximity effect, this becomes particularly demanding when dense patterns with closely positioned features must be fabricated. Figure 2.11 presents an example of nanoscale morphologies after exposure and development of high-density gratings with various interline distances (pitches) in PMMA resist on a silicon wafer [38, 43]. From the figure, it is evident that the potential to fabricate a quality grating is strongly dependent on both the exposure dose and the interline distance. Thus, for 70 nm pitch, all the images present well developed gratings, with the exception of Fig. 2.11d that corresponds to the high area dose of 125 μC/cm^2. For 40 and 50 nm gratings, promising morphologies are seen in Fig. 2.11n, o, k for the doses from 50 to 75 μC/cm^2. For 30 nm interline distance, only Fig. 2.11m for 60 μC/cm^2 exhibits a promising morphology. The other images in Fig. 2.11 show various damaging influences. For example, underexposure, when the clearance depth of exposed lines is insufficient to generate a grating pattern, is manifested by a low contrast in Fig. 2.11m, q, r. The other extreme regime, overexposure, when the pattern is damaged by excessive clearance of PMMA, is evident in Fig. 2.11a, b. Mild signs of overexposure are also visible in Fig. 2.11c, e. Another common type of morphology damage is the collapse of interline resist walls. Examples of collapsed gratings are seen in Fig. 2.11d, f, g, and also to some extent in Fig. 2.11j, k. It is noteworthy that collapse only occurs in gratings with 40 nm and larger pitch. In 30 nm gratings the limiting mechanism is different as illustrated in Fig. 2.11e, i. In these cases, the grating is partly or entirely destroyed by redistribution of PMMA that tends to form islands at irregular locations. Formation of such globular islands or percolation networks is known to occur in immiscible liquids that undergo a phase transition. Since mixtures of PMMA fragments with most common EBL developers have regimes of limited miscibility, a phase separation can occur [45, 46].

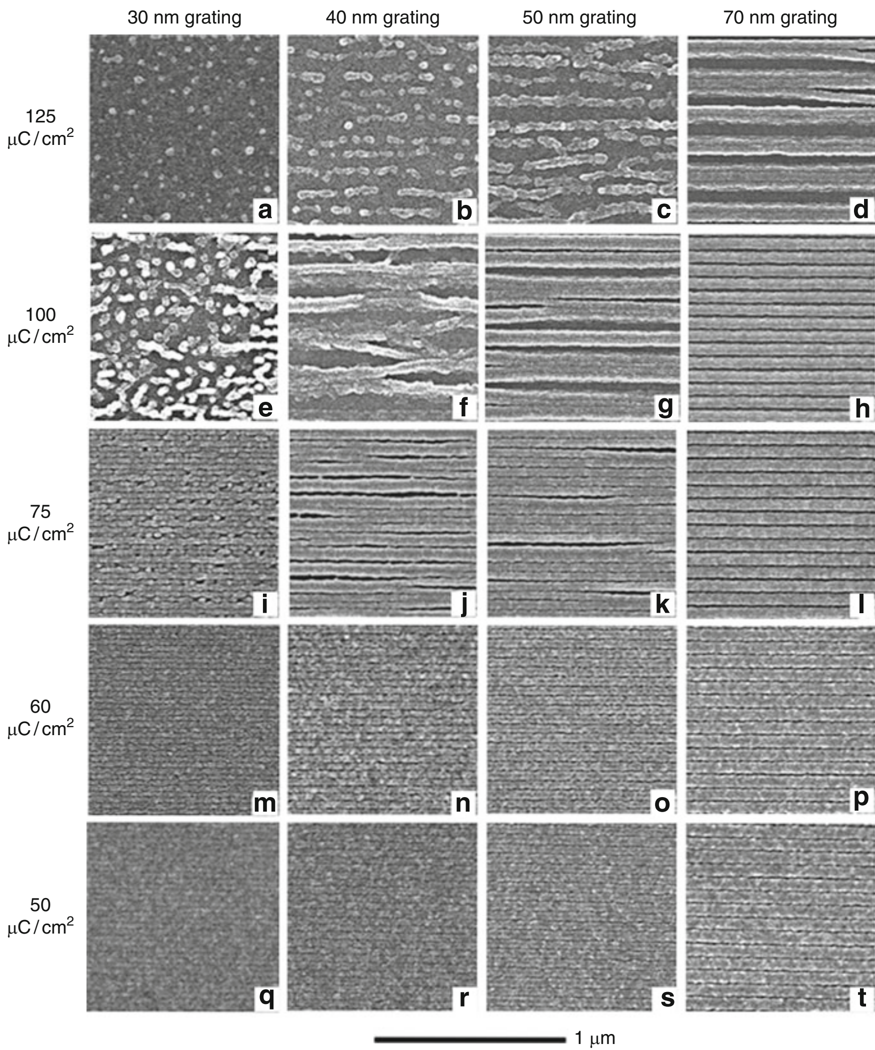

Fig. 2.11 SEM images of 30, 40, 50, and 70 nm gratings fabricated in a 65-nm thick PMMA layer on a silicon substrate, with 10 keV exposure at various area doses. The gratings were developed for 5 s in a 1:3 MIBK:IPA solution at room temperature. The lateral size of all images is 1 μm × 1 μm [43]. The average area doses are related with the line doses by $d_{area} = d_{line}/\lambda$, where λ is the interline distance (grating pitch)

Figure 2.12 summarizes the observed morphologic regimes for various grating periods and exposure doses. In the low dose regime, the limiting factor is underexposure, whereas at increased doses, the patterns degrade through phase separation or collapse. The densest gratings, with periods of 20 and 30 nm, degrade through phase separation, and the gratings with periods of 40 nm and larger rather tend to collapse. At even higher doses, gratings become overexposed. It can be seen

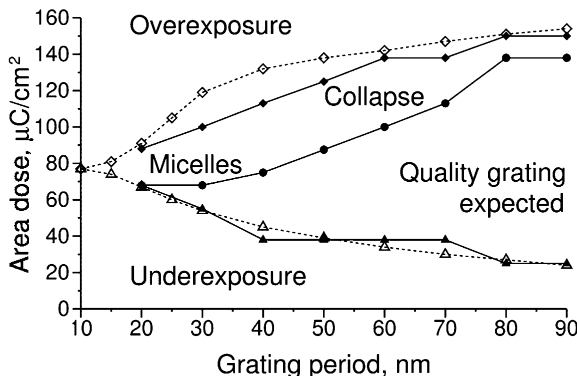

Fig. 2.12 Diagram of the characteristic morphologies in PMMA for various grating periods and area exposure doses using 10 keV voltage. Filled symbols represent experimental results from Fig. 2.9: *triangles* denote the boundary for underexposure (insufficient clearance); *diamonds* denote the boundary for overexposure (excessive clearance), and *circles* indicate the boundary for collapse or phase separation producing micellized patterns. Open symbols show the results of numerical modeling [43]

that the window of favourable exposure doses at which quality gratings can be expected decreases rapidly when the grating pitch decreases.

The width of the applicable dose window represents the robustness of the process [29, 38]. A large dose window means that the fabrication process has a better reproducibility, and also has greater controllability over the line width and aspect ratio. The minimum size of nanostructures for which a reasonable dose window is attained characterizes the resolution. For example, from Fig. 2.12 it follows that the highest resolution attainable at the experimental conditions considered corresponds to approximately 15 nm half-pitch representing the average line width. The minimum applicable doses can be associated with the sensitivity of the EBL process.

2.2.1 Temperature Dependence of Applicable Process Window

As already mentioned, the resist's development occurs through the removal of relatively low-weight fragments from the intensely exposed regions. This removal can be described as a kinetic diffusion-like process, with a molecular mobility represented by diffusivity, $D \sim n^{-\alpha} \exp(-U/kT)$, where U is the activation energy and the factor $n^{-\alpha}$ describes the mobility of fragments of size n in a medium whose properties are represented by power α. In most polymers, α varies from 1 in dilute solutions of small molecules to 2 for longer polymer chains in denser melts [27–29].

As noted in Fig. 2.6, in exposed PMMA, the average size of fragments $<n>$ is a function of both the exposure dose and location. For moderate exposure doses, the mean size of fragments $<n>$ is inversely proportional to the local probability of

scissions, which in turn is related with exposure dose d, so that $<n> \sim 1/d$, and the diffusivity of fragments in exposed PMMA can be approximately described by,

$$D = cd^{\alpha} \exp(-A/kT) \tag{2.1}$$

where c is a location-dependent model coefficient of proportionality [29].

In Refs. [29, 31], for an example of a dense periodic grating in PMMA, it was demonstrated that the boundary applicable doses for quality nanofabrication, d_{min} and d_{max}, depend on temperature as follows,

$$d_{\text{min,max}} = d^{ref}_{\text{min,max}} \exp\left(-\frac{U}{\alpha k}\left(1/T - 1/T^{ref}\right)\right) \tag{2.2}$$

where '*ref*' indicates reference values for the minimum and maximum applicable doses d_{min} and d_{max}. In Fig. 2.13, (2.2) is compared with the experimental temperature dependencies for the doses d_{min} and d_{max} in a 70 nm pitch grating exposed with 10 keV electrons, and developed at various temperatures for 5s and 20s. The boundary doses determined experimentally for $-15°$C development were used for reference in this example, and the estimated value $U/\alpha = 0.22$ eV was employed. It can be seen that (2.2) describes very well the broadening of the applicable dose window with the decrease of the development temperature. The lower boundary of the applicable dose window d_{min} (shown by solid lines in Fig. 2.13) can be interpreted as the dose at which PMMA fragments in the intensely exposed trenches are mobile enough to be removed over the time of development. The maximum applicable dose d_{max} (dashed lines) is, in turn, determined by molecular diffusion processes occurring in the walls. From Fig. 2.13, it is evident that both boundary doses d_{min} and d_{max} decrease with temperature, i.e. the process sensitivity increases at higher temperatures of development.

The regions between the solid and dashed lines in Fig. 2.13 represent the favorable dose windows where quality gratings may be fabricated. It can be seen that the width of the applicable dose window, $d_{max} - d_{min}$, increases strongly with

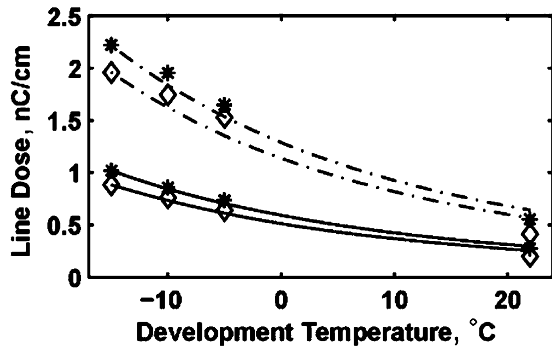

Fig. 2.13 Comparison of theoretical temperature dependencies for minimum (*solid lines*) and maximum (*dashed lines*) applicable exposure doses for a 70 nm pitch grating in PMMA exposed with 10 keV electrons. The symbols show the experimental data for development times of 5 s (*stars*) and 20 s (*diamonds*) [29]

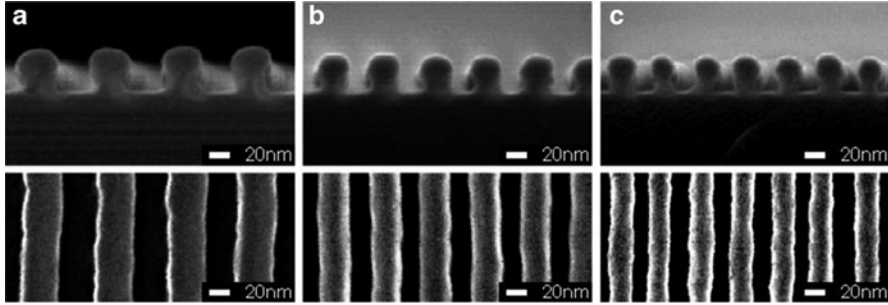

Fig. 2.14 Cross-section and top-view SEM micrographs showing examples of optimized dense nanoscale gratings fabricated in PMMA using a Raith 150 system with 10 keV voltage, and employing various development temperatures: (**a**) RT, 70 nm pitch; (**b**) −10°C, 50 nm pitch; and (**c**) −15°C, 40 nm pitch [29]

the *decrease* in the temperature of development. Thus, decreasing the development temperature from room temperature (RT) to −15°C results in an increase in the applicable line dose window by more than five times. This indicates a strong improvement in the EBL process robustness when decreasing the development temperature from RT to −15°C.

As an example of this increase in nanoscale resolution with decreasing temperature of development, Fig. 2.14 shows the highest resolution grating structures obtained in Ref. [29] by exposing 47–55 nm thick layers of PMMA to 10 keV electrons, for various development temperatures. It can be seen that RT development yields 33 ± 2 nm wide trench lines in a grating with a 70 nm pitch (a). With −10°C development, 20 ± 2 nm lines in a 50 nm pitch grating could be fabricated (b). This line width was further improved to 15 ± 2 nm in a 40 nm pitch grating at −15°C temperature (c).

One can conclude that the minimal resolved feature size significantly decreases with decrease of the development temperature from RT down to −15°C. This is consistent with the observed trend of broadening of the applicable dose windows, and can be explained by the kinetics of fragment mobility during resist dissolution. However, this advantage is accompanied by a drop in the process sensitivity. Reaching increased resolution and high sensitivity at the same time requires a trade-off involving co-optimization of several process conditions.

2.2.2 Interdependence of Exposure Dose and Development Time

Considering the resist development as a kinetic process involving diffusion of fragments from exposed resist into solvent, it is natural to expect the duration of development to be a control factor. The trend is illustrated by Fig. 2.15a, where the minimum (solid lines) and maximum (dashed lines) applicable doses, determined experimentally in a 50 nm grating pattern in PMMA, are shown as functions of time

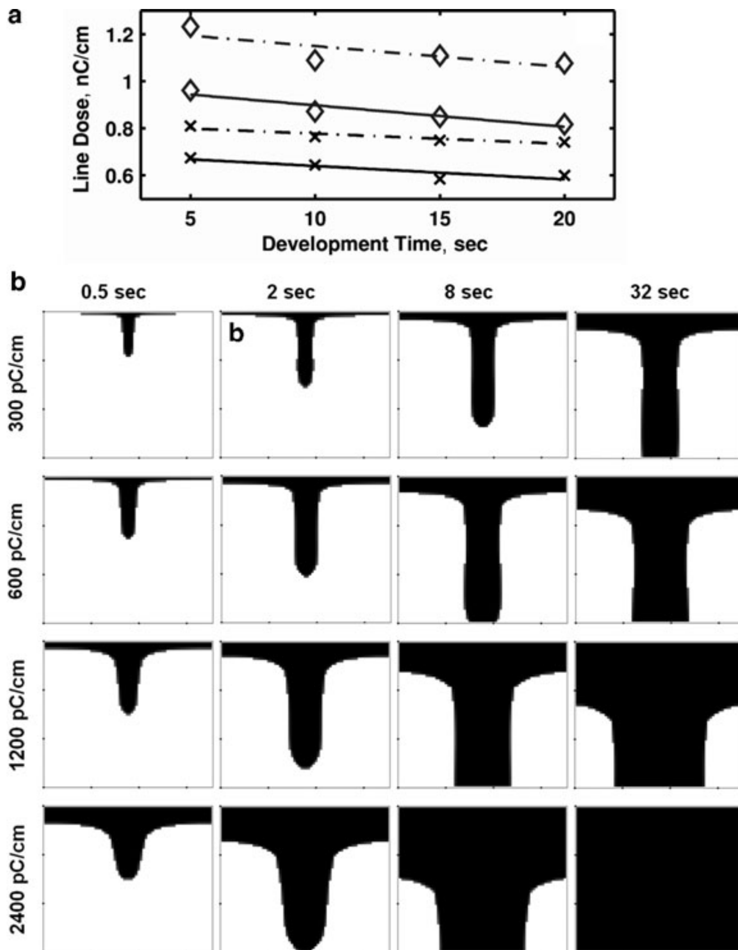

Fig. 2.15 (**a**) The applicable dose windows for 50 nm pitch gratings in PMMA showing minimum (*solid lines*) and maximum (*dashed lines*) line doses for quality patterning. The symbols indicate the temperature of development −5°C (*crosses*) and −15°C (*diamonds*) [29]. (**b**) Computed resist clearance profiles in a periodic grating with a 70 nm pitch exposed with 10 keV voltage with various line doses, and developed at −15°C for various durations. The width of all boxes is 70 nm, and the height is 60 nm. White denotes undissolved PMMA, and black denotes clearance [47]

of development at various temperatures. It can be seen that both the minimum and maximum boundaries show a moderate decrease with the development time. A minor to moderate decrease of the applicable dose window with the development time was also reported [38].

Figure 2.15b clarifies the interdependence of the exposure dose and development time, employing the results of recent kinetic modeling [47]. The figure presents a set of computed cross-sectional profiles in a grating with a 70 nm pitch, exposed

with various line doses, and developed during 0.5, 2, 8, and 32 s at −15°C. Some of the profiles appear to be close in terms of trench width despite the different process conditions. This is not surprising considering that assuming the Fick law for diffusion, removal of the resist is associated with the diffusion length of PMMA fragments $(Dt)^{1/2}$, where the effective diffusivity D is given by (2.1). As a result, for the width of the development trench Δx one can expect the proportionality $\Delta x \sim d\, t^{1/2}$, where d is dose and t is time. This indicates that optimal dose and time are related by an inverse proportionality, and should be selected simultaneously for optimal performance of EBL at the nanoscale.

2.2.3 The Exposure Voltage Factor

The initial energy of incident electrons plays an important role for the exposure process due to several factors. First, the inelastic collision cross-section decreases roughly in proportion to an increase in electron energy [19, 26, 48]. In positive resists such as PMMA, this decreases the number of chain scissions per electron at higher voltages. The resulting impact on the sensitivity of increasing the voltage from 3 to 30 keV is illustrated in Fig. 2.16. Both the minimum and the maximum applicable exposure doses increase approximately in proportion to the voltage, resulting in a significantly lower sensitivity for 30 keV than for 10 and 3 keV. In a general case, the decrease in sensitivity is an unwanted effect since it leads to lower throughput.

However, Fig. 2.16 also shows that increasing the electron energy results in a dramatic increase of the applicable dose windows. The reason for this is that electrons with higher energies undergo less forward scattering and as a result, the beam broadens less [11, 31]. This is illustrated in Fig. 2.3, which presents the computed distributions of small (1–12 monomers) fragments in PMMA with exposed parallel lines [38]. Cross-sectional profiles obtained in resists exposed with different voltages are presented in Fig. 2.17. The grating exposed with

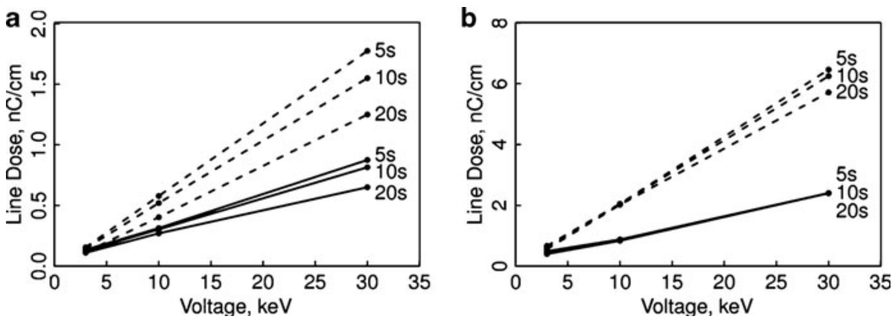

Fig. 2.16 Applicable line dose windows for 70 nm pitch gratings in for 3, 10, and 30 keV exposure voltages and different durations of development at RT (**a**) and at −15°C (**b**) [38]. The initial PMMA thickness was 55 nm. The meaning of the solid and dashed lines is as in Fig. 2.15

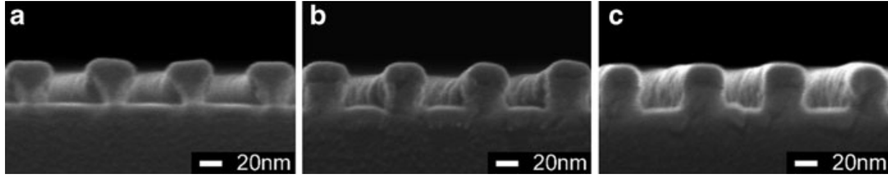

Fig. 2.17 SEM images of cross- sectional profiles for 70 nm pitch gratings fabricated at 3 keV (**a**), 10 keV (**b**), and 30 keV (**c**) voltages [31]

3 keV shows pronounced undercuts because of strong forward scattering of electrons, whereas 30 keV exposures produce almost straight interline walls. The low voltage tapered structures are more susceptible to pattern collapse, leading to reduced dose window. However, strong forward scattering of low energy electrons, which is usually believed to be the major resolution-limiting factor, may alternatively be employed to create nanoscale three-dimensional profiles in the resist [49] as is also demonstrated in the next section.

One more aspect to be mentioned in relation to the voltage, is its impact on the proximity effect. High energy electrons penetrate deeper into the substrate and can spread laterally due to backscattering. This gives rise to a significant proximity effect. The higher doses required at high energies compound this problem. In contrast, ultra low voltage electrons in the 1–3 keV regime deposit most of their energy within the resist, decreasing dramatically the proximity effect and also resulting in less substrate damage [11, 48].

2.3 Optimized EBL Processes: Examples

2.3.1 Low-kV, Cold Development PMMA Processing

As described in Sect. 2.2.3, 3 keV and lower voltage EBL has the advantages of higher sensitivity, lower substrate damage and proximity effect [11, 31, 48]. Furthermore, the strong forward scattering resulting in resist undercuts such as seen in Fig. 2.17a can be turned in an important processing advantage for metallization and lift-off patterning [49]. Conventionally, bi-layer resist schemes were used for metallization and lift-off at deep nanoscale [50–52]. A lower resolution resist layer would be coated first, followed by a higher resolution resist layer on top. When patterned, the resolution difference would yield a comparatively wider opening on the bottom resist layer as illustrated in Fig. 2.18. After subsequent metallization, this scheme would allow the solvent to access all areas of the trench and lift-off the PMMA resist layers without leaving any resist scum sticking to the substrate or deposited metal.

In contrast to using a bi-layer scheme, one can use a simpler single resist scheme by exploiting the re-entrant profiles created by scattering of low energy electrons. Using a single resist layer has two obvious advantages: (a) a thinner resist layer

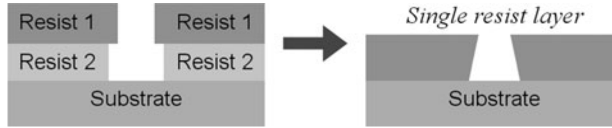

Fig. 2.18 Undercuts created in PMMA by using low-kV EBL enables replacement of bi-layer resist schemes (*left*) with a simpler single-resist layout (*right*)

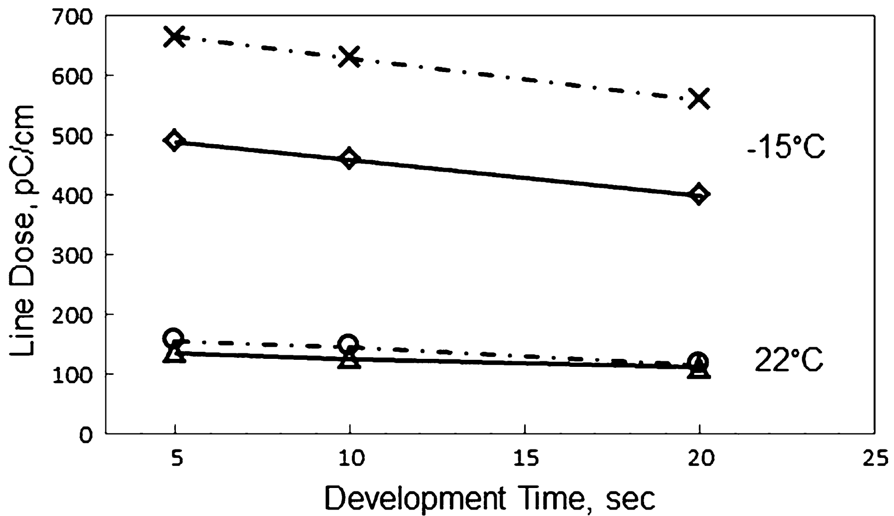

Fig. 2.19 Comparison of dose windows for 3 keV exposure voltages developed at room temperature (*triangles and circles*) vs. at −15°C (*diamonds and crosses*). The grating pitch is 70 nm and resist is 55 nm

allows a higher resolution since the aspect ratio requirement isn't as demanding, and (b) co-optimization of exposure doses and development conditions is simplified.

The advantages of using low voltage EBL are overcast by a major limitation: generally, the dose window for high-resolution, high-density gratings is very narrow for even thin resist layers. This property greatly affects the robustness of the EBL nanofabrication process i.e., small variations may lead to failure of the process. A useful work-around to this limitation is the use of cold development [38]. Figure 2.19 compares the dose windows for a 70 nm pitch grating in a 55 nm thick PMMA layer developed at room temperature and at −15°C. Cold development results in a dramatic increase in the applicable dose window by approximately an order of magnitude; however, this advantage is accompanied by a drop in the exposure sensitivity.

Using low-voltage exposure of PMMA in conjunction with cold development provides an extremely efficient and straightforward process of nanofabrication [29, 31, 38]. For example, at a PMMA thickness of 55 nm, the smallest grating pitch

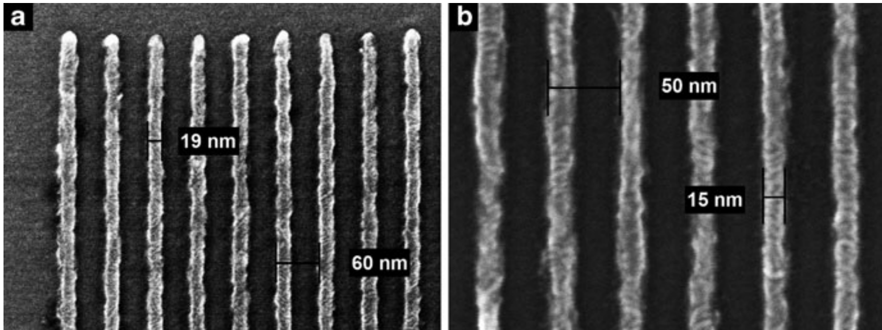

Fig. 2.20 (**a**) 20 nm wide Cr lines in a 60 nm pitch grating, and (**b**) 15 nm wide Cr lines in a 50 nm pitch grating, both fabricated by 3 keV exposure of a single layer of PMMA 950 K resist, and developed at −15°C

that our group could fabricate using 3 keV EBL at room temperature development was 70 nm. However, by using −15°C cold development, 50 nm pitch gratings could be realized with sub-20 nm line features after metallization and lift-off. Figure 2.20a, b shows sub-20 nm wide Cr lines in 60 and 50 nm pitch gratings, respectively, fabricated by deposition of a 12 nm thick layer of chromium on patterned PMMA features and subsequent lifted-off in acetone with ultrasonic agitation [53].

As described previously, one of the advantages of low-voltage EBL is the reduction of proximity effect [11, 48]. To illustrate this, Fig. 2.20a shows a corner of a Cr metallized grating array with uniform features at the edges of the pattern. This demonstrates the ability to fabricate high-resolution structures using low-voltage EBL in conjunction with cold development without the use of any proximity effect correction (PEC) routines [54–56]. The usage of low development temperature also improves the resistance of nano-patterned PMMA against post-exposure degradation such as wall collapse and fusion. In conclusion, cold development provides a significant number of advantages to a low-voltage EBL process such as higher resolution, larger dose window, pattern robustness, etc., at the expense of some loss in resist sensitivity.

2.3.2 Taking Control of PMMA: Sub-20 nm Wide Bridge Designs

As an example of optimized, PMMA-based ultrahigh resolution lithographic device fabrication, in this section we describe a recent improvement of existing silicon carbon nitride (SiCN) bridge resonator fabrication technology [57, 58] employing a low-voltage, cold development EBL process [53].

Figure 2.21 summarizes the improved process flow. In brief, an initial plasma enhanced chemical vapour deposition step is used to deposit a 50 nm thick SiCN layer followed by an anneal which sets the film to a tensile stress. A 45 nm thick PMMA film is then spun-cast, exposed at 3 keV, and developed at −15°C in MIBK: IPA 1:3. A 12 nm thick Cr layer is deposited by e-beam evaporation followed by an

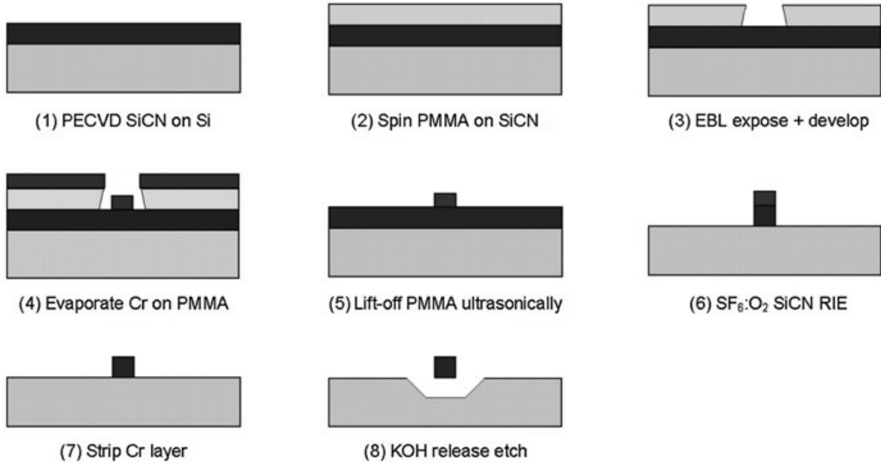

Fig. 2.21 Process flow outlining the steps used to fabricate doubly-clamped SiCN bridge resonators using a low voltage EBL and cold development process

ultrasonically assisted lift-off in acetone for 3 min. The Cr layer is used as an etch mask for the SiCN reactive ion etch (RIE) which is conducted with a 4:1 SF_6:O_2 recipe. Finally, after stripping the Cr layer, a wet release etch is conducted using hot KOH. Further processing details can be found in Ref. [53]

As a result of the above process, large arrays of nanoscale SiCN double-clamped bridge resonators could be fabricated with lengths between 1 and 20 μm. Figure 2.22 shows a representative micrograph of a 5 μm long bridge structure with a thickness of 50 nm and a width of 16 nm. In general, the minimum achievable linewidth of the bridge depended upon the desired length. The narrowest bridges with sub-15 nm widths could only be fabricated for lengths of up to 2 μm; bridges with widths between 14 and 18 nm could only be fabricated for lengths of up to 10 μm; and beyond that widths of 20–28 nm were required. Bridges with more demanding length to width aspect ratios failed due to mechanical fracture.

In Fig. 2.23 it can be seen that the bridge widths can be very finely controlled by applied electron beam single pixel line (SPL) dose for 1 μm long resonators. As the dose is reduced, the bridge width decreases: for doses of 2.0, 1.6, and 1.5 nC/cm, 16 ± 2 nm wide, 13 ± 3 nm wide, and 11 ± 5 nm wide bridges are fabricated, respectively. As the bridge widths decrease and approach 10 nm widths, the relative width non-uniformity strongly increases. At the smallest widths, small etch variations adversely affect the edge roughness.

An even more precise process control over the most critical part of the device, the clamping point, can be achieved with the usage of numerical modeling. The clamping point is a major factor in determining mechanical losses, so its fabrication is a key step to ensuring high resonator performance. In particular, any overhang or rounding at the corner is to be minimized. Considering the complexity of the interplay of many factors contributing to the EBL technique, being able to simulate

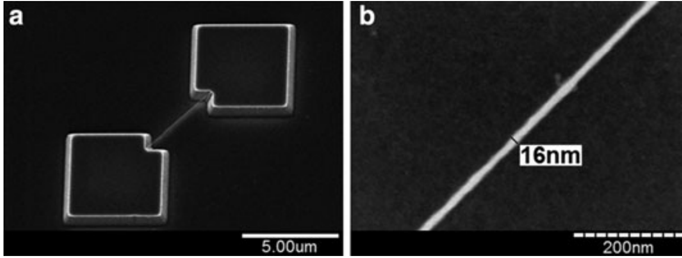

Fig. 2.22 A sub-20 nm wide, 5 μm long doubly-clamped SiCN resonator (**a**), and (**b**) a magnified image of the bridge showing a width of 16 ± 2 nm [53]

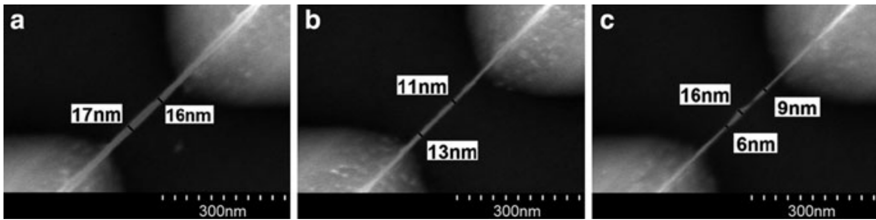

Fig. 2.23 Demonstrating control over the bridge widths: 1 μm long doubly-clamped SiCN bridges measuring (**a**) 16 ± 2 nm exposed at 2.0 nC/cm, (**b**) 13 ± 3 nm exposed at 1.6 nC/cm, and (**c**) 11 ± 5 nm exposed at 1.5 nC/cm [53]

all or some stages of the EBL process replaces time consuming and expensive cut-and-try experiments with a more efficient and rational, in-silico aided process design.

Figure 2.24 shows the user interface of the modeling tool and outlines the simulation procedure that was used to optimize the design of the clamping point in the resonator. This EBL simulator allows visualization of the electron beam exposure, fragmentation, and development of exposed positive tone resist, such as PMMA, on conductive substrates. In particular, 3D spatial maps of PMMA main chain scissions and 3D resist clearance profiles for given development conditions (duration, temperature) can be generated. More details on the EBL simulator can be found in Ref. [47].

Figure 2.25 demonstrates the results of the simulations and compares them to experimentally obtained results. A typical resonator clamping point is sketched in Fig. 2.25a and the results of simulation of the low-voltage exposure (3 keV) and cold development (−15°C) are presented in Fig. 2.25b, c, respectively. It can be seen that the numerically obtained results in Fig. 2.5c very accurately resemble the developed PMMA resist profile shown in Fig. 2.5d. The rounding of the clamping point seen in Fig. 2.25c, d arises because of the forward scattering of primary electrons.

The clamping point rounding results in an increase the overhanging area where undercuts occur after the final release etch. In Fig. 2.25e, the area where the SiCN

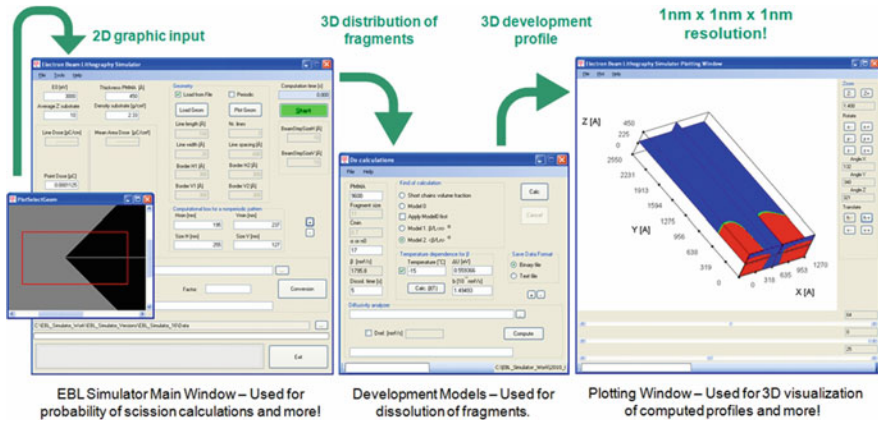

Fig. 2.24 Screen-shots of the EBL simulator user interface demonstrating the procedures of graphic input, simulation of the exposure (*chain scission*) and development, and visualization of the results. Further details on the simulation tool can be found in Ref. [47]

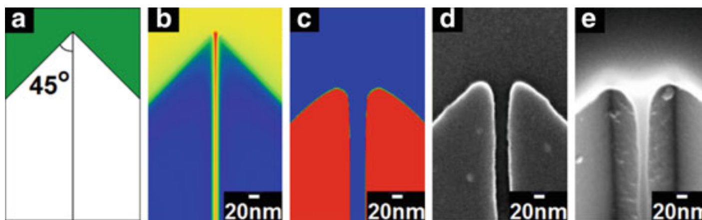

Fig. 2.25 (**a**) Sketch of a typical resonator clamping point design, (**b**) the computed yield of scission (*exposure plot*), (**c**) the computed dissolution profile (*development plot*), (**d**) a SEM image of the developed PMMA resist, and (**e**) a SEM image of the released SiCN resonator clamping point [53]

overhangs appears as the brighter parts around the clamping point. Generally, such overhangs contribute towards unwanted clamping losses and need to be avoided. To reduce the overhang around the clamping point, a number of alternative clamping designs were modelled and tested with the help of the EBL simulation tool. Designing and testing alternative clamping geometries provides greater flexibility than simple proximity effect correction (PEC) approaches, which are generally used to optimize the doses when complex structures involving multiple length scales are being fabricated.

Figures 2.26 and 2.27 illustrate two of the most successful designs. The first design (Fig. 2.26a) aims to sharpen the clamping point by defining a gap between the pad and resonator line at the design stage. This design exploits the movement of the resist-developer interface (the dissolution front) at the development stage such that the pad and resonator *just connect* yielding a sharp clamping point, provided the pad-resonator gap is optimized. An optimized gap of 170 nm was

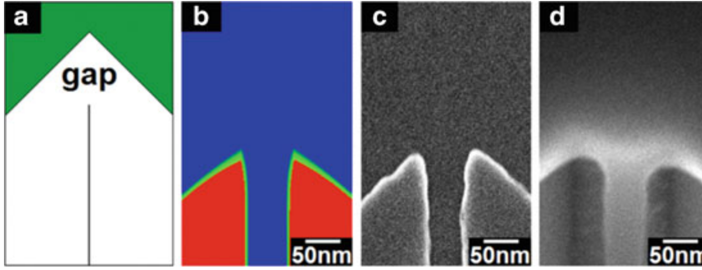

Fig. 2.26 (**a**) Diagram of an alternative clamping point design with an optimized gap of 170 nm between resonator and pad, (**b**) the final dissolution profile compared with (**c**) a SEM image of the developed PMMA resist showing sharper corners compared to Fig. 2.25d, and (**d**) a SEM image of the released SiCN resonator clamping point [53]

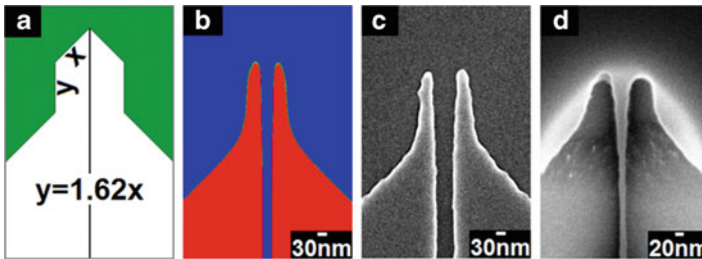

Fig. 2.27 (**a**) Diagram of an alternative clamping point design with an optimized side width of x = 165 nm, (**b**) the final dissolution profile compared with (**c**) a SEM image of the developed PMMA resist, and (**d**) a SEM image of the released SiCN resonator clamping point [53]

obtained by modelling, as shown in Fig. 2.26b, and experimentally realized, see Fig. 2.26c. After the release-etch, there still is some rounding in the device layer (Fig. 2.26d) as compared to the sharper corners seen in the resist layer in Fig. 2.26c; however, the result is better in comparison with Fig. 2.25e. One can hypothesize that the remaining rounding is due to the etchant contact angle and surface area minimization effects at the release etch stage. The second design (Fig. 2.26a) aims to isolate the resonator from the overhanging mass of the clamping point, and thus overcome the issue of the clamping point rounding. This design allows tuning the lengths of two sides such that an empty area is obtained around the beam. The two sides are related by the relation y = 1.618x. Through the help of the EBL simulator, an optimized value of x = 165 nm was obtained as shown in Fig. 2.26b and fabricated, see Fig. 2.26g. In this case after the release-etch, the overhanging area (the higher contrast and brighter part in Fig. 2.6d) is clearly disconnected from the resonator bridge.

One can conclude that employing low-voltage, cold development PMMA-based EBL process, complemented by in-silico aided optimization of the design, can be extremely efficient for ultrahigh resolution device fabrication.

2.3.3 Sub-10 nm Processing with HSQ

Employing polymer resist such as PMMA to fabricate sub-10 nm features in dense array configurations, although possible in principle, approaches the limit related to the size of the molecules, which challenges the attainable levels of uniformity and reproducibility. In the last decade, there has been significant interest in the usage of an alternative inorganic EBL resist hydrogen silsesquioxane (HSQ), which has shown considerable potential at the 10-nm scale (see for example review paper [59]). HSQ is a negative tone resist which cross-links to form an insoluble silica-like structure, although at significantly higher doses than required to process positive tone PMMA.

Many HSQ developers have been used such as TMAH – $(CH_3)_4NOH$ [60–66], NaOH [62, 66, 67], KOH [66, 68] and LiOH [66]. All of the above developer solutions are hydroxides i.e., they are basic solutions. Some of the optimization strategies included increasing developer strength from 2.38% TMAH to 25% TMAH, increasing the development time to 1 min [60], increasing the TMAH developer temperature to 50°C [63], adding NaCl solutions to NaOH [62, 67, 69] adding various salt solutions to all the above developers etc. [66]. The aforementioned optimization strategies have all yielded contrast improvements.

Apparently, TMAH-based development simultaneously provides the highest resolution while offering the greatest number of testable optimization strategies. Table 2.2 features three development recipes based on TMAH. Recipe (A) is a standard HSQ development recipe utilizing room temperature 25% TMAH developer diluted in water. Recipe (B) uses hot 50°C 25% TMAH developer [61–65]. Recipe (C) is a modified three step development recipe [70] in which a dilute hydrofluoric acid dip is incorporated between two hot TMAH development stages. Recipe (C) will be described in more detail later.

Figure 2.28 compares results for 50 nm pitch HSQ gratings exposed and developed using two different strategies. The gratings shown in Fig. 2.28a were exposed at 10 keV using a dose of 1.25 nC/cm and developed at room temperature. The gratings shown in Fig. 2.28b were exposed at 30 keV using a dose of 4.2 nC/cm and developed at 50°C. The images show that (a) the line resolution is superior to what has been illustrated in Sect. 2.3.1 for PMMA, and (b) using a higher voltage and hot development allows access to a sub-10 nm resolution at the cost of a significant reduction in sensitivity. One can conclude that a higher (30 keV) exposure and hot (50°C) development option appears as the baseline optimized process to achieve sub-10 nm resolution for HSQ [71].

Table 2.2 Examples of development schemes useful for HSQ

Recipe	Developer formulation
(A)	75 s dip in 25% TMAH
(B)	75 s dip in 50°C 25% TMAH
(C)	75 s dip in 50°C 25% TMAH
	+30–60 s dip in 2000:1 H_2O:BOE
	+75 s dip in 50°C 25% TMAH

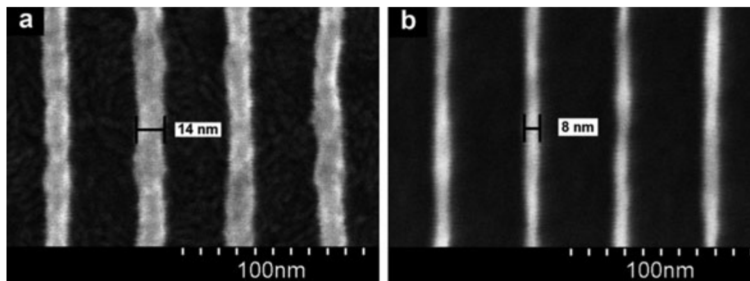

Fig. 2.28 Comparison of a 50 nm pitch HSQ grating developed at (**a**) room temperature, and at (**b**) 50°C, in 25% TMAH

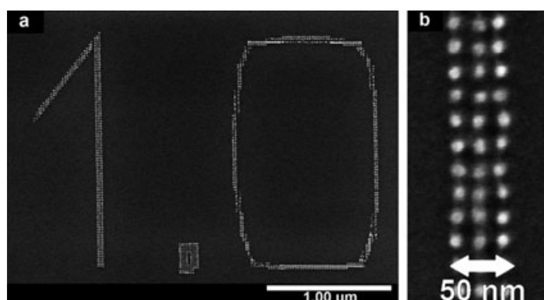

Fig. 2.29 Arbitrary area patterns (**a**) showing EBL rastering, and (**b**) magnified image of the rastering showing 10 nm diameter dots

While optimizing HSQ process, care must be taken regarding a number of conditions during the exposure and development stages. Thus at the exposure stage, beam step size is important. Since the resolution HSQ is superior to that of PMMA, both the single pixel line (SPL) and area step sizes must be chosen less than for PMMA. Figure 2.29a shows an arbitrary text written with a Raith 150^{TWO} EBL system using an area step size of 20 nm. As shown in the magnified image provided in Fig. 2.29b, the rastering spots approx. 10 nm in diameter are visible. A continuous exposure can be achieved with decreased step sizes of 2–10 nm.

After choosing a small enough beam step size, exposure dose selection is the next step. Figure 2.30 shows an area dose test pattern with squares exposed at successively higher doses. The dose factors are marked above each square. At the extremes, either the dose is too low for pattern delineation, or the dose is too high and the pattern is severely distorted. In the middle, a window of applicable doses can be seen. In contrast to positive resists, selecting the minimum cross-linking dose would not work if the pattern is intended to be used as a masking layer for subsequent etching. In that case, the cross-link density may not be high enough to be a suitable etch mask. Thus with negative tome resists, the preferred dose is often the largest possible cross-linking dose before pattern distortion, as opposed to selecting the minimum clearance dose for positive tone resists.

The selection of the largest possible cross-linking dose, however, has a downside of the process of cross-linking becoming extremely sensitive to exposure by

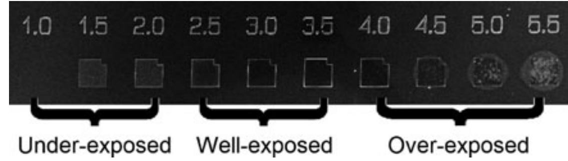

Fig. 2.30 Dose test for HSQ showing various exposure regimes

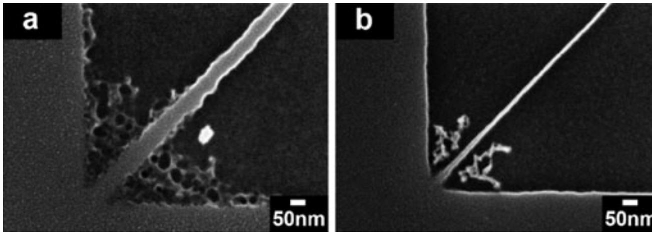

Fig. 2.31 SEM images of un-released SiCN masking layer at the pad-resonator interface developed using (**a**) standard TMAH recipe (A) with centre width 48 ± 5 nm, and (**b**) with modified hot TMAH-BOE-TMAH recipe (C) with centre width 15 ± 2 nm [71]

secondary and backscattered electrons. These proximity effects may cause unwanted partly-exposed siloxane-like scum [70–72] around pattern sidewalls and dense features as shown in Fig. 2.31a. Since the siloxane-like scum consists of an oxide, $HSiO_x$, it can be etched away using dilute HF rinse [70] which is also beneficial for the resist contrast as it prevents the development step from saturating [70] and also trims the patterns which enhances the resolution even further [72].

Additionally, hot development has also been reported to remove these partly cross-linked structures [63]. To solve the described issues, an alternative development scheme has been developed recently [71], see recipe (C) in Table 2.2. In this recipe, hot development is combined with HF-trimming or multi-step TMAH-HF-TMAH development. This combination helps to clean up the unwanted siloxane-like scum and also provide pattern trimming as shown in Fig. 2.31b. The trimming is estimated to be as high as 20 nm/min.

2.3.4 HSQ Resist as Etching Mask: 8 nm Wide Bridge

Exploiting the optimized HSQ based nano-patterning techniques discussed in Sect. 2.3.3, the SiCN resonator fabrication process discussed in Sect. 2.3.2 has been further improved [71]. By using HSQ both as the resist layer and the masking layer for the SiCN RIE, the resonator fabrication process has been simplified by eliminating the chromium metal layer, and its resolution has been enhanced to achieve sub-10 nm wide, microns long bridges. The highly optimized SiCN resonator fabrication process [71] is summarized in Fig. 2.32.

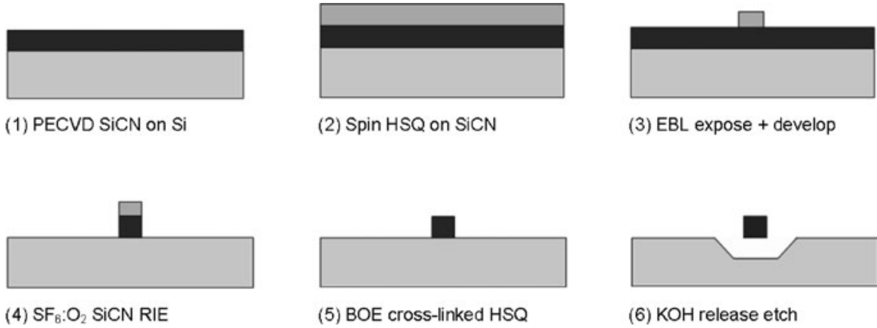

Fig. 2.32 Process flow outlining the steps used to fabricate doubly-clamped SiCN resonators using a HSQ mask (Adapted from Ref. [71])

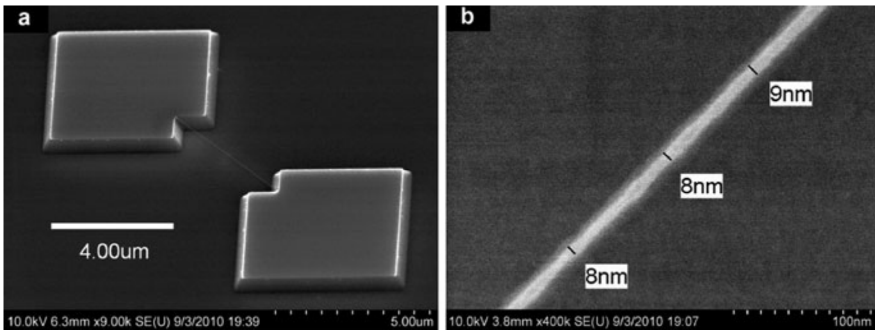

Fig. 2.33 A sub-10 nm wide, 5 μm long doubly-clamped SiCN resonator: (**a**) overview image, and (**b**) a magnified image of the bridge

After depositing and annealing a 50 nm thick SiCN layer on Si, a 25–30 nm thick HSQ layer is spin on top. The HSQ layer is exposed by 30 keV EBL and developed using the multi-step hot TMAH-HF-TMAH recipe (C) from Table 2.2 as described in Sect. 2.3.3. The cross-linked HSQ layer is used as an etch mask for the SiCN RIE and then is stripped off using a 30 s BOE. Finally the resonator is released in a 75°C 28.3% KOH bath saturated with IPA for short etch durations ranging from 30 to 45 s. Further details can be found in Ref. [71].

Figure 2.33a presents a SEM image of a typical sub-10 nm wide, 5 μm long doubly-clamped SiCN resonator with SiCN layer thickness of 50 nm. The EBL area and line doses used were 2.5 mC/cm^2 and 9 nC/cm respectively. Figure 2.33b is a magnified top-view SEM image of the bridge. The SEM image is taken from the centre of the resonator shown in Fig. 2.33a. The measured width of the bridge is 9 ± 1 nm. Bridges of similar resolution can also be obtained using single step room temperature recipe (A) or hot development recipe (B); however, this is inferior because a higher dose is required, the bridges are less uniform, and a presence of siloxane-like scum in the clamping area.

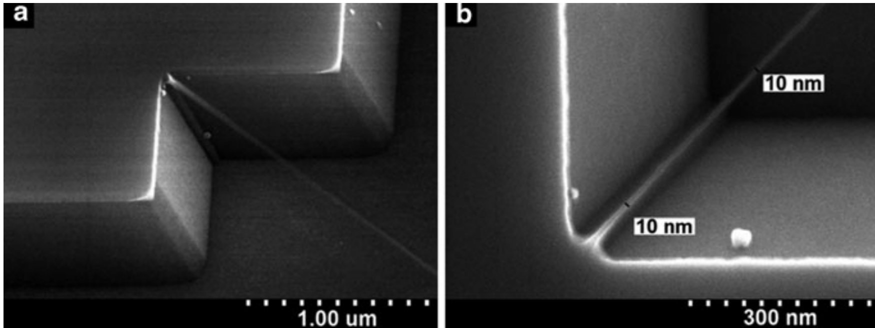

Fig. 2.34 SEM images of the clamping point: (**a**) tilt-view showing clamping features and release, and (**b**) top-view showing width uniformity

Figure 2.34a, b presents magnified SEM images of the resonator clamping point fabricated using recipe C from Table 2.2. Both figures show that little or no residual scum is visible at the clamping point and the surfaces and edges are very clean. The areas around the clamping point show only a minor overhanging. The bridges are suspended 400–600 nm above the silicon surface. Finally, both Figs. 2.33b and 2.34b show that the bridge width is uniform and less than 10 nm along its entire length. This demonstrates that by co-optimization of exposure and development conditions, proximity effects can be avoided or compensated without the use of complicated correction algorithms.

2.4 Insulating Substrates

Application areas such photonics, nanoelectronics, and bio-nano-electromechanical systems (bio-NEMS) often require fabrication of large, macroscopic-scale arrays of nanoscale features. Nanoimprint lithography has emerged as an efficient and low cost solution [73]. Ultraviolet nanoimprint lithography (UV-NIL), which involves an optical exposure, requires fabrication of transparent nanostructured masters. Dielectric materials appropriate for this purpose present a difficulty when employing EBL for their nanostructuring. Unlike with conducting and semiconducting substrates, polymeric resist layers such as PMMA on top of insulators accumulate charge during EBL exposure, which deflects the beam and distorts the pattern [74–76].

The solutions revolve largely around usage of conducting anti-charging layers. It has been demonstrated that thin (from 5 nm) overlayers of light metals such as Al, Cr, or Cu, can be functional when fabricating periodic grating patterns with a pitch up to 150–200 nm [77]. Such coatings, however, result in electron beam scattering in the metal layer and subsequent broadening of the exposure profile in the resist, which limits the resolution at the deep nanoscale. The technique also tends to decrease the process sensitivity [77].

An example of an alternative process where a metallic anti-charging layer is located underneath the resist is given in Fig. 2.35 [78]. In brief, a UV transparent fused silica (FS) substrates is coated with a sputtered 30 nm Al film, followed by spin coating a 60 nm layer of PMMA resist. In this PMMA/Al/FS scheme, the Al layer works as a charge conduction layer during e-beam exposure, and later, works as hard mask for pattern transfer into the FS substrate via glass etching. After 10 keV EBL exposure with a Raith 150 system and development of the PMMA, reactive ion etch (RIE) is carried out to transfer the pattern to the underlying Al layer.

As the next step, The EBL features from the Al layer are transferred to the fused silica substrate by a RIE process. The Al mask is then removed from the substrate. Figure 2.36a, b shows the examples of an Al grating pattern with composed of ~40 nm lines with a ~60 nm interline distance, and a corresponding grating pattern in fused silica, respectively. An edge roughness is visible that occurs because nanocrystalline grains are formed during Al deposition by sputtering. Although

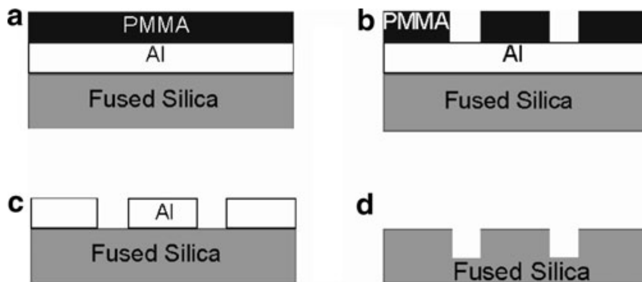

Fig. 2.35 NIL mask fabrication schemes: (**a**) glass substrate is coated with Al and PMMA. (**b**) Patterns generated by e-beam exposure are realized in PMMA, (**c**) which is then transferred to the Al layer using dry etch with PMMA acting as the etch mask. (**d**) Patterns are then transferred to the glass substrate via glass etch process with the Al layer acting as hard mask. Finally the Al mask is removed from the fused silica surface

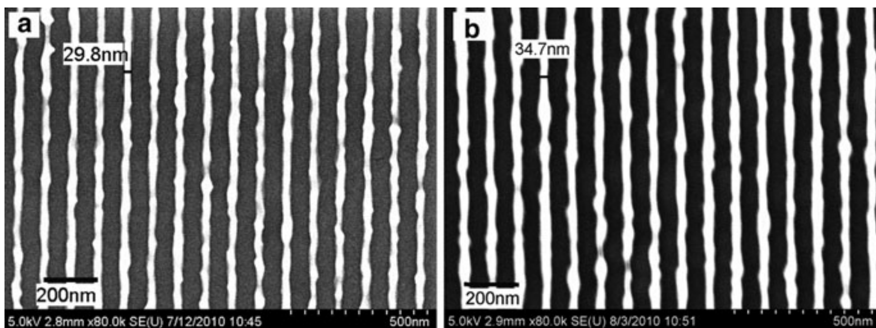

Fig. 2.36 100 nm pitch gratings with less than 40 nm wide lines realized in the Al layer (**a**), and released in a fused silica substrate (**b**). An edge roughness resulting from metal grains is visible

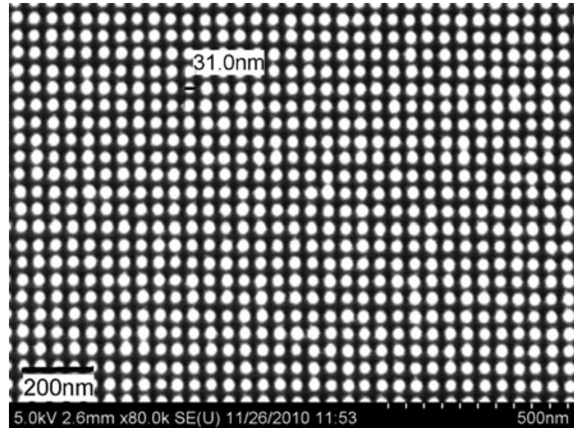

Fig. 2.37 Array of posts with 50 nm × 50 nm pitch fabricated in a fused silica substrate employing a conducting polymer aquaSAVE [81] of top of PMMA as an anti-charging layer

the grain size can be deceased by carefully selecting the conditions of deposition and the metal [79], the roughness in the released FS pattern caused by the metallic grains is a quite common challenge of this approach.

A different solution is to use a layer of a conducting polymer instead of a metal layer, in which case the polymer is usually deposited of top of the EBL resist [80]. Figure 2.37 presents an example of dense arrays of posts, only ~30 nm across and with 50 nm pitch, released in fused silica [78]. In this process, a 90 nm thick film of PMMA was coated with 70 nm of water soluble, conducting polymer (aquaSAVE from Mitsubishi Rayon [81]), and the pattern was generated using 30 kV e-beam exposure with a Raith 150$^{\mathrm{TWO}}$ system. After removal of the anti-charging layer and development of PMMA, an 8 nm film of Cr was sputter deposited and then lifted-off in an ultrasonic bath. The patterns realized in Cr were then transferred to the FS substrate by RIE. In comparison with metallic layers deposited on top of the resist, polymers introduce less beam broadening, offering a stronger potential in an increase of resolution at the deep nanoscale. The lift-off stage, however, turned out to be somewhat pattern sensitive, with the quality of the released pattern of same nominal size varied depending on the geometry [78]. Clearly, further process optimization effort, including the insight from numerical modeling, is needed to fully realize the potential of EBL on insulating substrates.

2.5 Summary

EBL is a complex process with many interacting parameters that affect the quality of the resulting nanofabricated structures and the robustness of the process. An approach has been presented for mapping regimes within which successful results can be achieved, with a particular emphasis on PMMA as a model resist. An analytic model of exposure and development has been presented as a tool to aid this analysis. Use of low energy EBL has been explored to improve sensitivity and

reduce proximity effects. Cold development has been shown to improve process windows and resolution, particularly in concert with low energy exposure. Application of these tools and techniques to the improvement of an isolated nanoscale bridge structure and a dense, insulating nanoimprint lithography master have been presented.

Acknowledgements The authors are grateful for the support of the Natural Sciences and Engineering Research Council of Canada, the National Institute for Nanotechnology, the Alberta Ingenuity Fund, Raith GmbH, and the University of Alberta NanoFab.

References

1. McCord MA, Rooks M. Electron beam lithography. In: Rai-Choudury P, editor. Handbook of microlithography, micromachining and microfabrication, vol. 1. Bellingham: SPIE; 1997. ISBN 978-081-942-378-8.
2. Nabity J, Compbell LA, Zhu M, Zhou W. E-beam nanolithography integrated with scanning electron microscope. In: Zhou W, Wang ZhL, editors. Scanning microscopy for nanotechnology: techniques and applications. 1st ed. New York: Springer; 2006. ISBN 978-144-192-209-0.
3. Wu CS, Makiuchi Y, Chen CD, In: Wang M, editors. Lithography. High-energy electron beam lithography for nanoscale fabrication. Croatia: InTech; 2010, ISBN 978-953-307-064-3.
4. Liddle JA, Berger SD. Proc SPIE. 2014;2014:66–76.
5. Pfeiffer HC, Stickel W. Future Fab Intl. 2002;12:187.
6. Mapper Lithography, Delft, www.mapperlithography.com
7. Raith GmbH, Dortmund, www.raith.com
8. Goldstein J, Newbury DE, Joy DC, Lyman CE, Echlin P, Lifshin E, Sawyer L, Michael JR. Scanning electron microscopy and X-ray microanalysis. 3rd ed. New York: Springer; 2003. ISBN 978-030-647-292-3.
9. Jeol electron beam lithography, Tokyo, www.jeol.com/PRODUCTS/SemiconductorEquipment/ElectronBeamLithography/tabid/99/Default.aspx
10. Vistec electron beam GmbH, Jena, www.vistec-semi.com
11. Lee YH, Browing R, Maluf N, Owen G, Pease RFW. J Vac Sci Technol B. 1992;10:3094–8.
12. Yang H, Fan L, Jin A, Luo Q, Gu C, Cui Z. In: Proc. 1st IEEE Intl. Conf. Nano/Micro Engg. & Molec. Sys. Jan 2006, Zhuhai, p. 391–4.
13. Kyser DF, Viswanathan NS. J Vac Sci Technol. 1975;12:1305–8.
14. Brewer G, editor. Electron-Beam Technology in Microelectronic Fabrication. New York: Academic; 1980. 978-012-133-550-2.
15. Kamp M, Emmerling M, Kuhn S, Forchel A. J Vac Sci Technol B. 1999;17:86–9.
16. Chang THP. J Vac Sci Technol. 1975;12:1271–5.
17. Lo CW, Rooks MJ, Lo WK, Isaacson M, Craighead HG. J Vac Sci Technol B. 1995;13:812–20.
18. Mun LK, Drouin D, Lavallée E, Beauvais J. Microsc Microanal. 2004;10:804–9.
19. Wu B, Neureuther AR. J Vac Sci Technol B. 2001;19:2508–11.
20. Showa Denko ESPACER, www.showadenko.us
21. Hatzakis M. J Electrochem Soc. 1969;116:1033–7.
22. ZEONREX electronic chemicals, Japan http://www.zeon.co.jp/index_e.html
23. Nishida T, Notomi M, Iga R, Tamamura T. Jpn J Appl Phys. 1992;31:4508–14.
24. Olynick DL, Cord B, Schipotinin A, Ogletree DF, Schuck PJ. J Vac Sci Technol B. 2010;28:581–7.
25. Bilenberg B, Schøler M, Shi P, Schmidt MS, Bøggild P, Fink M, Schuster C, Reuther F, Gruetzner C, Kristensen A. J Vac Sci Technol B. 2006;24:1776–9.

26. Aktary M, Stepanova M, Dew SK. J Vac Sci Technol B. 2006;24:768–79.
27. Masaro L, Zhu XX. Prog Polym Sci. 1999;24:731–75.
28. Miller-Chou BA, Koenig JL. Prog Polym Sci. 2003;28:1223–70.
29. Mohammad MA, Fito T, Chen J, Aktary M, Stepanova M, Dew SK. J Vac Sci Technol B. 2010;28:L1–4.
30. Tanaka T, Morigami M, Atoda N. Jpn J Appl Phys. 1993;32:6059–64.
31. Mohammad MA, Fito T, Chen J, Buswell S, Aktary M, Stepanova M, Dew SK. Micr Eng. 2010;87:1104–7.
32. Lee K, Bucchignano J, Gelorme J, Viswanathan R. J Vac Sci Technol B. 1997;15:2621–6.
33. Yasin S, Hasko D, Ahmed H. J Vac Sci Technol B. 1999;17:3390–3.
34. Kupper D, Kupper D, Wahlbrink T, Bolten J, Lemme M, Georgiev Y, Kurz H. J Vac Sci Technol B. 2006;24:1827–32.
35. Namatsu H, Yamazaki K, Kurihara K. J Vac Sci Technol B. 2000;18:780–4.
36. Goldfarb D, de Pablo J, Nealey P, Simons J, Moreau W, Angelpoulos M. J Vac Sci Technol B. 2000;18:3313–7.
37. Wahlbrink T, Kupper D, Georgiev Y, Bolten J, Moller M, Kupper D, Lemme M, Kurz H. Microelectron Eng. 2006;83:1124–7.
38. Mohammad MA, Fito T, Chen J, Buswell S, Aktary M, Dew SK, Stepanova M. In Wang M editors, Lithography. The interdependence of exposure and development conditions when optimizing low-energy EBL for nano-scale resolution. Croatia: InTech; 2010, ISBN 978-953-307-064-3.
39. Ocola LE, Stein A. J Vac Sci Technol B. 2006;24:3061–5.
40. Häffner M, Heeren A, Fleischer M, Kern DP, Schmidt G, Molenkamp LW. Microelectron Eng. 2007;84:937–9.
41. Cord B, Lutkenhaus J, Berggren KK. J Vac Sci Technol B. 2007;25:2013–6.
42. Yan M, Choi S, Subramanian KRV, Adesida I. J Vac Sci Technol B. 2008;26:2306–10.
43. Mohammad MA, Dew SK, Westra K, Li P, Aktary M, Lauw Y, Kovalenko A, Stepanova M. J Vac Sci Technol B. 2007;25:745–53.
44. Cord B, Yang J, Duan H, Joy DC, Klingfus J, Berggren KK. J Vac Sci Technol B. 2009;27:2616–21.
45. Hasko DG, Yasin S, Mumatz A. J Vac Sci Technol B. 2000;18:3441–4.
46. Yasin S, Hasko DG, Khalid MN, Weaver DJ, Ahmed H. J Vac Sci Technol B. 2004;22:574–8.
47. Stepanova M, Fito T, Szabó Zs, Alti K, Adeyenuwo AP, Koshelev K, Aktary M, Dew SK. J Vac Sci Technol B. 2010;28:C6C48–57.
48. Schock K-D, Prins FE, Strähle FES, Kern DP. J Vac Sci Technol B. 1997;15:2323–6.
49. Brünger W, Kley EB, Schnabel B, Stolberg I, Zierbock M, Plontke M. Microelectron Eng. 1995;27:135–8.
50. An L, Zheng Y, Li K, Luo P, Wu Y. J Vac Sci Technol B. 2005;23:1603–6.
51. Cord B, Dames C, Berggren KK, Aumentado J. J Vac Sci Technol B. 2006;24:3139–43.
52. Yang H, Jin A, Luo Q, Li J, Gu C, Cui Z. Microelectron Eng. 2008;85:814–7.
53. Mohammad MA, Guthy C, Evoy S, Dew SK, Stepanova M. J Vac Sci Technol B. 2010;28: C6P36–41.
54. Anbumony K, Lee S. J Vac Sci Technol B. 2006;24:3115–20.
55. Leunissen L, Jonckheere R, Hofmann U, Unal N, Kalus C. J Vac Sci Technol B. 2004;22:2943–7.
56. Ogino K, Hoshino H, Machida Y, Osawa M, Arimoto H, Maruyama T, Kawamura E. Jpn J Appl Phys. 2004;43:3762–6.
57. Fischer LM, Wilding LMN, Gel M, Evoy S. J Vac Sci Technol B. 2007;25:33–7.
58. Fischer LM, Wright VA, Guthy Cz, Yang N, McDermott MT, Buriak JM, Evoy S. Sens Actuators B. 2008;134:613–7.
59. Grigorescu AE, Hagen CW. Nanotechnology. 2009;20:292001.
60. Fruleux-Cornu F, Penaud J, Dubois E, Francois M, Muller M. Mater Sci Eng C. 2005;26:893–7.

61. Chen Y, Yang H, Cui Z. Microelectron Eng. 2006;83:1119–23.
62. Yang H, Jin A, Luo O, Gu C, Cui Z. Microelectron Eng. 2007;84:1109–12.
63. Haffner M, Haug A, Heeren A, Fleischer M, Peisert H, Chasse T, Kern DP. J Vac Sci Technol B. 2007;25:2045–8.
64. Choi S, Jin N, Kumar V, Adesida I, Shannon M. J Vac Sci Technol B. 2007;25:2085–8.
65. Ocola LE, Tirumala VR. J Vac Sci Technol B. 2008;26:2632–5.
66. Kim J, Chao W, Griedel B, Liang X, Lewis M, Hilken D, Olynick D. J Vac Sci Technol B. 2009;27:2628–34.
67. Yan M, Lee J, Ofuonye B, Choi S, Jang JH, Adesida I. J Vac Sci Technol B. 2020;28:C6S23–7.
68. Lauvernier D, Vilcot J-P, Francois M, Decoster D. Microelectron Eng. 2004;75:177–82.
69. Yang JKW, Berggren KK. J Vac Sci Technol B. 2007;25:2025–9.
70. Lee H-S, Wi J-S, Nam S-W, Kim H-M, Kim K-B. Vac Sci Technol B. 2009;25:188–92.
71. Mohammad MA, Dew SK, Evoy S, Stepanova M. Microelectron Eng. 2011;88:2338–41.
72. Tiron R, Mollard L, Louveau O, Lajoinie E. J Vac Sci Technol B. 2007;25:1147–51.
73. Schift H. J Vac Sci Technol B. 2008;26:458–80.
74. Liu W, Ingino J, Pease RF. J Vac Sci Technol B. 1995;13:1979–83.
75. Satyalakshmi KM, Olkhovets A, Metzler MG, Harnett CK, Tanenbaum DM, Craighead HG. J Vac Sci Technol B. 2000;18:3122–5.
76. Joo J, Jun K, Jacobson JM. J Vac Sci Technol B. 2007;5:2407–11.
77. Samantaray CB, Hastings JT. J Vac Sci Technol B. 2008;26:2300–5.
78. Muhammad M, Buswell SC, Dew SK, Stepanova M. J Vac Sci Technol B. 2011;29:06F304.
79. Bhuiyan A, Dew SK, Stepanova M. Comput Commun Phys. 2011;9:49–67.
80. Dylevwicz R, Lis S, De La Rue RM, Rahman F. J Vac Sci Technol B. 2010;28:817–22.
81. aquaSAVE Electronic Conductor, Mitsubishi Rayon America Inc., New York, http://www.mrany.com/data/HTML/20.htm

http://www.springer.com/978-3-7091-0423-1

Nanofabrication
Techniques and Principles
Stepanova, M.; Dew, S. (Eds.)
2012, VIII, 344 p., Hardcover
ISBN: 978-3-7091-0423-1